Evaluation and Optimization of Modulation Strategies of a Dual-Active-Bridge Converter for Electrolyzers

DESHMUKH, R.S.; Rituraj, G.; Bauer, P.; Vahedi, H

DOI
10.1109/OJIES.2025.3647490

Publication date
2025

Document Version
Final published version

Published in
IEEE Open Journal of the Industrial Electronics Society

Citation (APA)
DESHMUKH, R. S., Rituraj, G., Bauer, P., & Vahedi, H. (2025). Evaluation and Optimization of Modulation Strategies of a Dual-Active-Bridge Converter for Electrolyzers. *IEEE Open Journal of the Industrial Electronics Society*, *7*, 55-71. https://doi.org/10.1109/OJIES.2025.3647490

IEEE Open Journal of the
Industrial Electronics Society

Received 14 November 2025; accepted 16 December 2025. Date of publication 23 December 2025;
date of current version 5 January 2026. The review of this article was arranged by Associate Editor Danilo I. Brandao.

Digital Object Identifier 10.1109/OJIES.2025.3647490

Evaluation and Optimization of Modulation Strategies of a Dual-Active-Bridge Converter for Electrolyzers

ROHAN SHAILESH DESHMUKH (Graduate Student Member, IEEE), GAUTAM RITURAJ (Member, IEEE), PAVOL BAUER (Senior Member, IEEE), AND HANI VAHEDI (Senior Member, IEEE)

[1]Delft University of Technology, 2628 CD Delft, The Netherlands

CORRESPONDING AUTHOR: ROHAN SHAILESH DESHMUKH (e-mail: r.s.deshmukh@tudelft.nl).

ABSTRACT Electrolyzers operate as nonlinear low-voltage high-current loads, presenting significant challenges for power conversion systems. This article investigates state-of-the-art modulation schemes for the dual-active-bridge (DAB) converters, focusing on their performance and interaction with electrolyzer loads in electrolysis applications. The behavior of electrolyzers is compared with that of conventional constant voltage loads across various modulation schemes, using peak primary transformer current as the evaluation metric at three power levels: 1, 10, and 100 kW. A peak current optimization strategy tailored for electrolysis applications is proposed. Based on this, an optimized operating trajectory for the DAB converter during electrolysis is identified for each power level. The optimization results are validated experimentally using a 1-kW 20-kHz prototype, and through MATLAB simulations for the 10- and 100-kW systems. The proposed approach achieves peak current reductions of up to 15.75% at 100 W for the 1-kW system, 42.71% at 1 kW for the 10-kW system, and 60% at 10 kW for the 100-kW system, demonstrating its effectiveness in improving DAB converter performance for electrolysis applications.

INDEX TERMS DC–DC converter, dual active bridge (DAB), DAB converter, electrolyzer, hydrogen, modulation, optimization.

I. INTRODUCTION

Green hydrogen is rapidly gaining attention as a key enabler of a sustainable energy transition [1], [2]. It is produced by splitting water into hydrogen and oxygen using renewable energy sources (RESs), such as solar, wind, or hydropower. Unlike conventional hydrogen production from natural gas, green hydrogen offers a clean alternative, generating no greenhouse gas emissions during either production or use [3], [4]. Currently, electrolysis stands as the leading method for producing green hydrogen, carried out using specialized equipment known as electrolyzers.

Power electronics play a key role in connecting RESs to electrolyzers. In most cases, electrolyzers are connected to conventional ac power systems through a single ac–dc conversion stage, sometimes with an additional dc–dc stage that utilizes a bulky low-frequency transformer. However, electrolyzers can also connect directly to dc distribution systems. Unlike ac setups, dc systems use high-frequency (HF) transformers inside their dc–dc converters. These transformers are much smaller and cheaper than the low-frequency ones used in ac systems. They can also operate at much higher switching speeds, which shift current harmonics to higher frequencies, reducing their impact. Due to these advantages, dc-based electrolyzer systems have significant potential compared to ac-based ones. This study focuses on electrolyzers connected to dc distribution systems.

DC–DC converters designed for electrolyzers must meet several requirements, which include (not limited to) [5], [6]:

1) high efficiency over a wide operating range;
2) high power density;
3) low electromagnetic interference;
4) smaller output current ripple;
5) low cost;
6) reliability in the case of power switch failures.

TABLE 1. Comparison of Existing Literature and the Proposed Work

Ref	DC Grids	EV Charging	SST	Aerospace	ESS	Electrolysis	Modulation Comparison
[8]–[10]	✓						
[11]		✓					✓
[12]–[16]		✓					
[17]–[20]			✓				
[21], [22]				✓			
[23]–[25]					✓		
[26]					✓		✓
[27]–[32]						✓	
This work						✓	✓

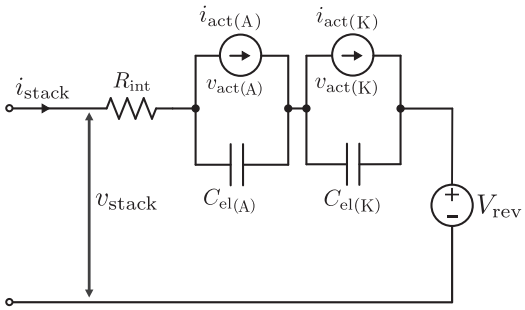

FIGURE 1. Electrical model of an alkaline electrolyzer.

Along with the specified requirements, the converter being designed must integrate galvanic isolation that meets ISO:22734:2020 and ISO:19880-1:2020 standards. Given the characteristics of electrolysis, the converter must also operate at low voltages with exceptionally high currents. Based on the literature review presented in [7], isolated dc–dc converter topologies are well suited for this type of application. Among these, the dual-active-bridge (DAB) converter stands out as a promising power electronics interface for electrolyzers, and it has received considerable research attention among isolated dc–dc converters.

However, it is essential to note that the DAB converter's basic topology alone cannot meet all the outlined requirements. Achieving the necessary functionality requires the integration of switching schemes or modulation strategies, which significantly influence the performance of the DAB converter. Table 1 provides a comparison of prior research on DAB converters with the present study, organized by application [8], [9], [10], [11], [12], [13], [14], [15], [16], [17], [18], [19], [20], [21], [22], [23], [24], [25], [26], [27], [28], [29], [30], [31], [32]. The majority of research on DAB converters has focused on applications in dc grids and electric vehicle (EV) charging, followed by applications in solid-state transformers (SSTs), energy storage systems (ESSs), electrolysis, and aerospace. Nonetheless, there is limited comprehensive analysis and comparison of different modulation strategies from the perspective of specific applications, which complicates the selection of suitable strategies for various operating conditions. For example, only one study has compared modulation strategies for EV charging [11] and ESS applications [26], while no comparative research exists for electrolysis applications.

This work emphasizes the DAB converter operation and optimization under different modulation strategies for electrolyzers and has the following key contributions.

1) It examines DAB converter performance within electrolysis using the three primary phase-shift modulation schemes—single phase shift (SPS), dual phase shift (DPS), and triple phase shift (TPS), providing expressions for output power and state currents for various operating modes of DPS and TPS tailored for electrolysis, with detailed illustrations of each mode.
2) While the SPS phase-shift ratio is straightforward to determine, calculating phase-shift ratios for DPS and TPS schemes is more complex. A simple peak current optimization method using the "fmincon" function in MATLAB is presented for the DPS and TPS methods for electrolysis. Detailed steps of this optimization process are provided along with parameter selections.
3) A comparative analysis is performed to show the effect of electrolyzer load on the SPS, DPS, and TPS modulation schemes from the primary transformer peak currents context for three power ratings (1, 10, and 100 kW) of electrolyzer against a 500-V constant voltage (CV) load of the same power ratings.
4) An optimized operation for electrolysis is proposed for the modulation methods and for each power rating. This optimized operation is compared against the conventional SPS modulation scheme, highlighting its benefit.

The rest of this article is organized as follows. Section II provides the electrical model of an alkaline electrolyzer. Section III presents the DAB converter operation and the analysis of SPS, DPS, and TPS modulation schemes from the context of electrolysis. Section IV presents the peak current optimization scheme for electrolysis, which determines the phase-shift ratios for DPS and TPS schemes. Furthermore, this scheme is extended to determine an optimal trajectory to operate the converter during electrolysis. Section V presents a comparative analysis of SPS, DPS, and TPS modulation schemes for electrolysis and CV loads across the three rated powers (i.e., 1, 10, and 100 kW). Section VI presents the experimental results for the 1-kW prototype and simulation results for the 10- and 100-kW systems. Finally, Section VII concludes this article.

II. ELECTROLYZER MODEL

Several modeling approaches have been proposed in the literature [33], [34], [35], [36]. For this work, the model presented in [35] is selected, as it provides both static and dynamic modeling of an alkaline electrolyzer. As illustrated in Fig. 1, the electrolyzer stack voltage consists of four key potentials: the reversible stack potential, activation potential, ohmic potential, and diffusion potential.

To streamline the modeling process, the following assumptions have been made.

1) The diffusion potential is negligible.

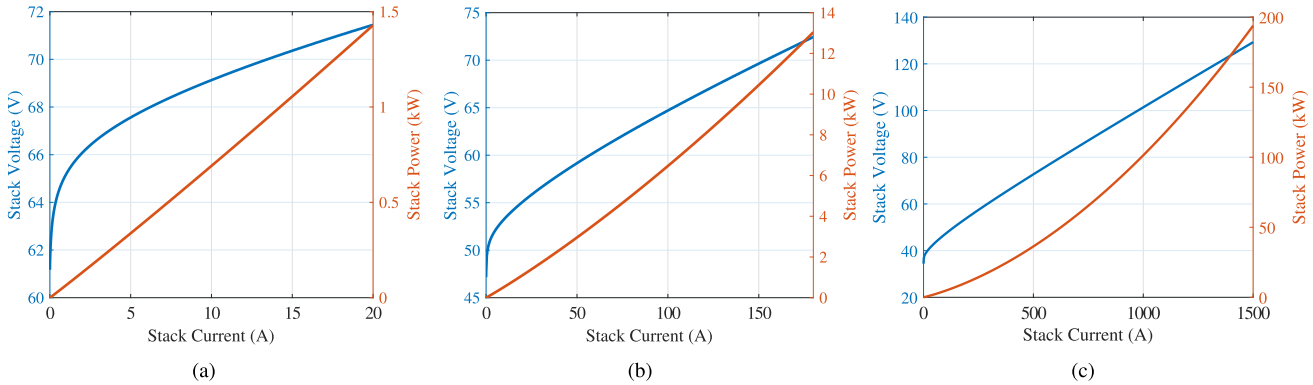

FIGURE 2. Electrical characteristics of electrolyzer considered in this work. (a) 1 kW. (b) 10 kW. (c) 100 kW.

2) The activation currents for both electrodes are considered the same as the stack current. Therefore, the static characteristics of the electrolyzer are used.
3) Temperature-dependent constants and area-specific-resistance values, which can only be obtained experimentally, have been used directly from [35].

Equation (1) defines the reversible stack potential. It exhibits the thermodynamic phenomena in the electrolysis reaction. Equations (2) and (3) define the electrode activation potentials for anode and cathode, respectively. This potential refers to the double-layer effect formed at the cell's cathode [37].

Finally, (4) refers to the ohmic potential, which can be defined as the voltage drop across the internal resistance (electrolyte) between the two electrodes

$$V_{\text{rev}} = N_{\text{s}}\left(V^{0}_{\text{rev,T}_{\text{c}}} + \frac{RT_{\text{c}}}{zF}\log\left(\frac{(P_{\text{abs}} - P_{\text{v(elec)}})^{1.5}}{a_{\text{we}}}\right)\right) \tag{1}$$

$$v_{\text{act(A)}} = sN_{\text{s}}\ln\left(\frac{i_{\text{act(A)}}}{t} + 1\right) \tag{2}$$

$$v_{\text{act(K)}} = vN_{\text{s}}\ln\left(\frac{i_{\text{act(K)}}}{w} + 1\right) \tag{3}$$

$$V_{\text{int}} = N_{\text{s}} i_{\text{stack}} R_{\text{int}} = N_{\text{s}} i_{\text{stack}} \frac{r}{A_{\text{elect}}} \tag{4}$$

where V_{rev} is the reversible cell voltage, V. $V^{0}_{\text{rev,T}_{\text{c}}}$ is defined as the temperature-dependent reversible voltage, V. R is known as the universal gas constant, J · K^{-1}mol^{-1}. T_{c} is the cell temperature, K. P_{abs} is the absolute pressure, bar. N_{s} is the number of series connected cells. z is the number of moles of electrons transferred for 1 mol of product. F is the Faraday constant, C·mol^{-1}. $P_{\text{v(elec)}}$ is the vapor pressure of KOH, bar. $a_{\text{H}_2\text{O,KOH}}$ is known as the water activity of KOH solution. s, t, v, and w are temperature dependent constants. $i_{\text{act(A)}}$ and $i_{\text{act(K)}}$ are activation currents for anode and cathode, respectively. r is the area-specific resistance of one of the electrolysis cells, Ω·m^2. i_{stack} is the stack current, A. A_{elect} is the electrode surface area, m^2. R_{int} is the internal resistance of the electrolyzer cell, Ω.

The total stack voltage of an alkaline electrolyzer can be obtained as the sum of the potentials mentioned in (1)–(4)

$$v_{\text{stack}} = V_{\text{rev}} + v_{\text{act(A)}} + v_{\text{act(K)}} + V_{\text{int}}. \tag{5}$$

The electrical characteristics of an alkaline electrolyzer for the considered rated powers of 1, 10, and 100 kW are shown in Fig. 2(a)–(c), respectively, for a temperature of 15 °C operating at a pressure of 5 bar.

III. ANALYSIS OF MODULATION STRATEGIES FOR ELECTROLYSIS

Fig. 3 illustrates the DAB converter, composed of two H-bridges: the H-HV consisting of switches, $Q_1 - Q_4$, and H-LV consisting of switches, $Q_5 - Q_8$. H-HV denotes the high-voltage-side bridge (referred to as the leading H-bridge), while H-LV denotes the low-voltage-side bridge (referred to as the lagging H-bridge). Each bridge is separated by an HF transformer for isolation in various applications.

A. SPS MODULATION

The SPS modulation scheme is one of the fundamental modulation schemes proposed for the DAB converter. It is the most widely used scheme [38], [39], [40], [41]. Fig. 4 showcases the SPS modulation scheme. Each switch of the DAB converter is operated at a fixed duty ratio of 50 %. However, the switches in the H-LV bridge are phase shifted by an angle ϕ or phase-shift duty ratio d with switches in the H-HV bridge as the reference. This way, power flow can be achieved from H-HV to H-LV or vice versa. The equations governing the operation of the DAB in the SPS modulation scheme are as follows:

$$P_{\text{o}} = \frac{(d \cdot (1-d)) \cdot V_{\text{DC}} \cdot kV_{\text{o}} \cdot N_{\text{t}}}{2 \cdot f_{\text{sw}} \cdot L} \tag{6}$$

$$N_{\text{t}} = \frac{V_{\text{DC}}}{V_{\text{o}}} \tag{7}$$

$$d = \frac{\phi}{\pi} \tag{8}$$

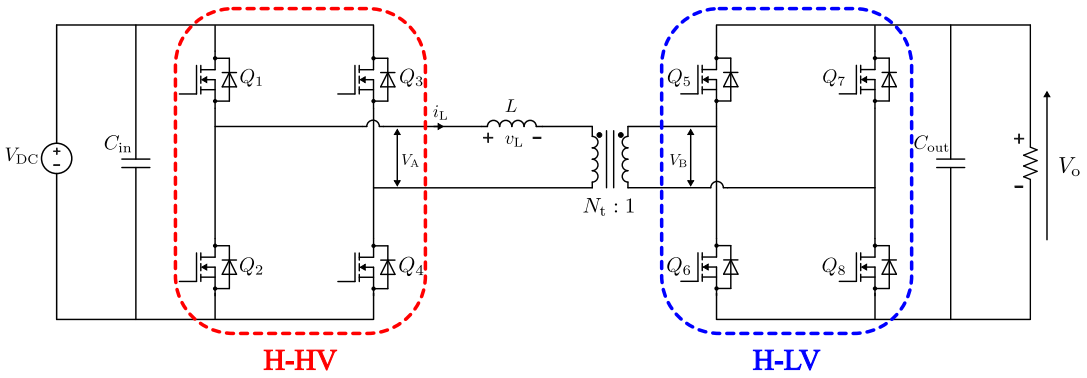

FIGURE 3. DAB converter.

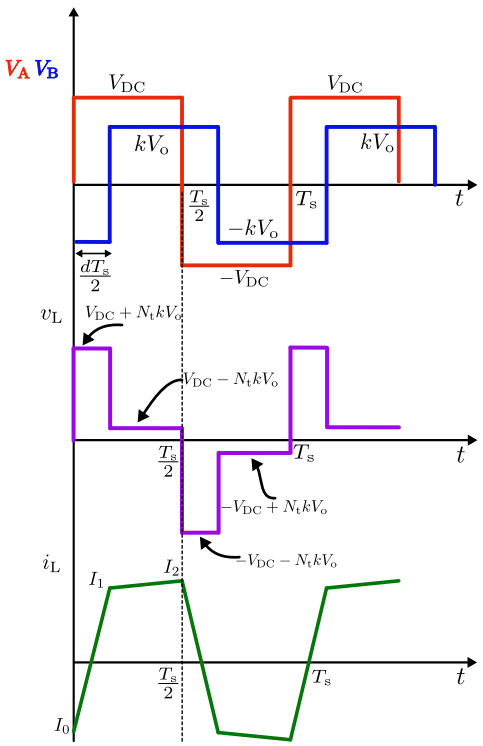

FIGURE 4. SPS modulation in the DAB converter.

where P_o is the output power, W. V_o is the nominal output voltage, V. V_{DC} is the input dc voltage, V. f_{sw} is the switching frequency, Hz. N_t is the primary to secondary turns ratio of the HF transformer. L is the series inductance, H. d is the phase-shift duty ratio, and ϕ is the phase angle, rad. k is the voltage gain, which is defined as the ratio of the stack voltage during electrolysis to the nominal output voltage of the DAB converter.

Furthermore, by substituting (5) into (6), we have

$$P_o = \frac{V_{DC} N_t N_s R d(1-d)}{2L f_{sw} z F}\left(T_c \log\left(\frac{(P_{abs} - P_{v,KOH})^{1.5}}{a_{we}}\right) + \frac{zF}{R}\left(V_{rev}^0 + s\log\left(\frac{i_{act(A)}}{t}+1\right) + v\log\left(\frac{i_{act(K)}}{w}+1\right) + V_{int}\right)\right). \quad (9)$$

Equation (9) showcases the relationship between the parameters of the DAB converter and the electrolyzer parameters [32]. It provides a strong indication that the choice of converter parameters can no longer be dependent purely on the voltage, current, and switching frequency, but also on parameters of the electrolyzer, such as the vapor pressure, water activity, activation currents, the internal resistance (the electrode–electrolyte interface behaves as a resistance), stack temperature, etc.

The small inertia and ease of realizing soft switching are some of the merits of SPS [42], making it an attractive modulation scheme for rated power operation, particularly considering the low-voltage and high-current nature of electrolysis.

B. DPS MODULATION

In the SPS modulation scheme, the power flow is determined by the phase-shift ratio, d. Due to the presence of only a single degree of freedom, the efficiency of this scheme begins to deteriorate when the voltage gain of the transformer deviates from unity [43]. This scenario occurs during electrolysis, too, since the voltage and current of the electrolyzer no longer remain fixed but remain dynamic as the reaction within the electrolyzer continues. This deviation of voltage gain from unity results in circulating currents or an increase in the reactive power within the converter, causing it to draw more current. Given the nature of electrolysis, i.e., a low-voltage and high-current process, the losses within the converter can increase significantly in such a scenario [44]. The DPS modulation scheme can address the issue of circulating currents, expand the soft-switching range, and decrease current stress [45], [46], [47].

Unlike the SPS modulation scheme, wherein only a single degree of freedom d exists, the DPS modulation scheme consists of two phase-shift ratios, d_1 and d_2. This work considers

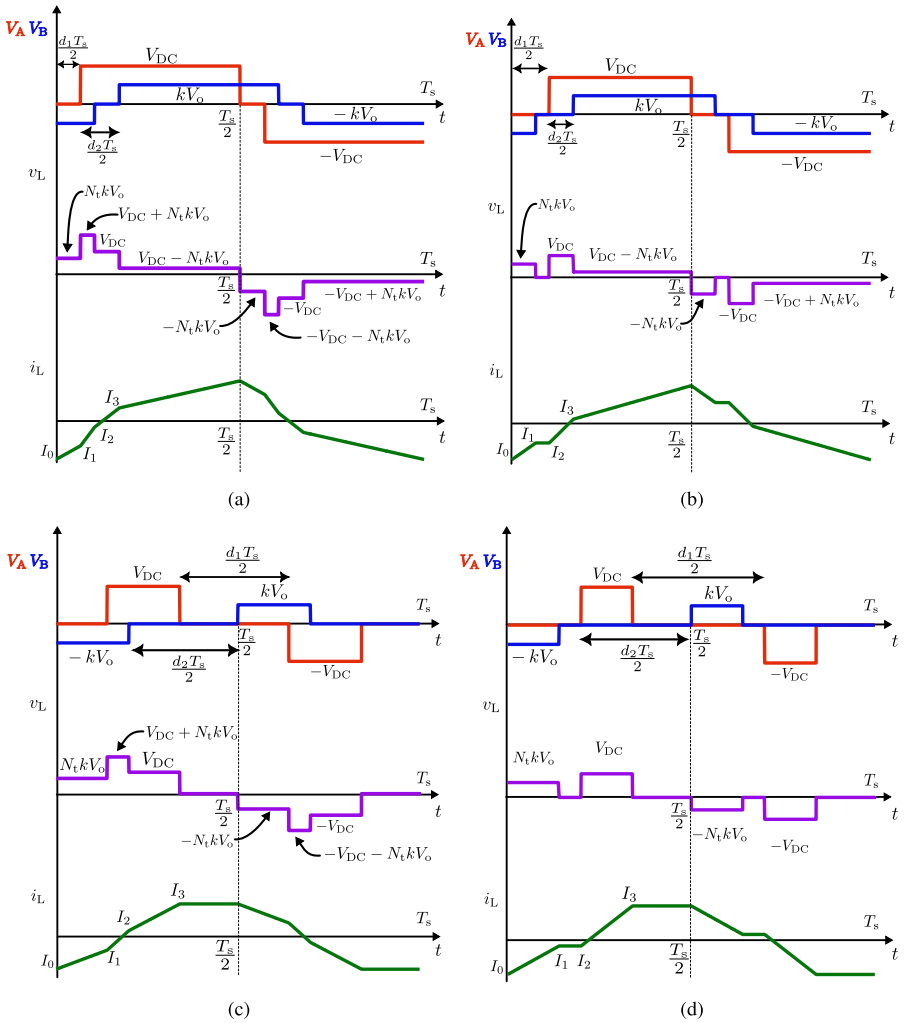

FIGURE 5. Modes of operation for the DPS modulation scheme. (a) Mode-I, ($d_1 + d_2 \leq 1, d_1 \leq d_2$). (b) Mode-II, ($d_1 + d_2 \leq 1, d_1 > d_2$). (c) Mode-III, ($d_1 + d_2 > 1, d_1 \leq d_2$). (d) Mode-IV, ($d_1 + d_2 > 1, d_1 > d_2$).

d_1 to be the inner phase-shift ratio while d_2 to be the outer phase-shift ratio. Both phase-shift ratios are lagging. Switch Q_4 is phase shifted by d_1, while switch Q_5 is phase shifted by d_2. Furthermore, switch Q_8 is phase shifted by $d_1 + d_2$. This sum of the inner and outer phase-shift ratios can also be defined as d_3 for the sake of simplicity. In this manner, phase-shift ratio d_3 is dependent on the inner and outer phase ratios. The presence of two degrees of freedom allows for better control of power flow. This work considers four modes.

Fig. 5 showcases the DPS modulation scheme along with the four modes of operation. For each mode, Table 2 provides the constraints for the phase-shift ratios, expressions for the state currents of the transformer (primary side), and expressions for the operating power of the converter for electrolysis, where $A = \frac{N_t V_o}{4 L f_{sw}}$.

C. TPS MODULATION

In the DPS modulation scheme, switch Q_8 is applied with a phase-shift ratio, d_3, which is the sum of the inner phase ratio, d_1, and the outer phase-shift ratio, d_2. By making d_3 independent of d_1 and d_2, an additional degree of freedom can be introduced for controlling the power flow. This is known as the TPS modulation scheme [16], [48], [49]. It is interesting to note that SPS and DPS are special cases of TPS modulation schemes. They can be implemented within the TPS modulation scheme with the following conditions:

$$d_1 = 0 \;\&\; d_2 = d_3 \rightarrow \text{SPS}$$

$$d_1 \neq 0 \;\&\; d_3 = d_1 + d_2 \rightarrow \text{DPS}.$$

In this work, three operating modes are considered. Fig. 6 showcases the TPS modulation scheme along with the three modes of operation. For each mode, Table 3 provides the constraints for the phase-shift ratios, expressions for the state currents of the transformer (primary side), and expressions for the operating power of the converter for electrolysis, where $A = \frac{N_t V_o}{4 L f_{sw}}$.

TABLE 2. Operating Modes in DPS Modulation

$d_1 + d_2 \leq 1$			
Mode - I ($d_1 \leq d_2$)		Mode - II ($d_1 > d_2$)	
$I_0 =$	$A(-k(d_1 + 2d_2 - 1) + d_1 - 1)$	$I_0 =$	$A(-k(d_1 + 2d_2 - 1) + d_1 - 1)$
$I_1 =$	$A(k(1 + d_1 - 2d_2) + d_1 - 1)$	$I_1 =$	$-A(d_1 - 1)(k - 1)$
$I_2 =$	$A(-k(d_1 - 1) - d_1 + 2d_2 - 1)$	$I_2 =$	$-A(d_1 - 1)(k - 1)$
$I_3 =$	$A(k(1 - d_1) + d_1 + 2d_2 - 1)$	$I_3 =$	$A(k(1 - d_1) + d_1 + 2d_2 - 1)$
$P_o =$	$kAV_{DC}(-d_1^2 - 2d_2^2 + 2d_2)$	$P_o =$	$kAV_{DC}d_2(-2d_1 - d_2 + 2)$
$d_1 + d_2 > 1$			
Mode - III ($d_1 \leq d_2$)		Mode - IV ($d_1 > d_2$)	
$I_0 =$	$A(d_1 - 1)(k + 1)$	$I_0 =$	$A(d_1 - 1)(k + 1)$
$I_1 =$	$A(d_1 - 1)(k + 1)$	$I_1 =$	$A(d_1 - 1)(k + 1)$
$I_2 =$	$A(k(1 + d_1 - 2d_2) + d_1 - 1)$	$I_2 =$	$A(1 - d_1)(k - 1)$
$I_3 =$	$A(-k(d_1 - 1) - d_1 - 1 + 2d_2)$	$I_3 =$	$A(1 - d_1)(k - 1)$
$P_o =$	$kAV_{DC}(1 - d_2)(d_2 - 2d_1 + 1)$	$P_o =$	$kAV_{DC}(d_1 - 1)^2$

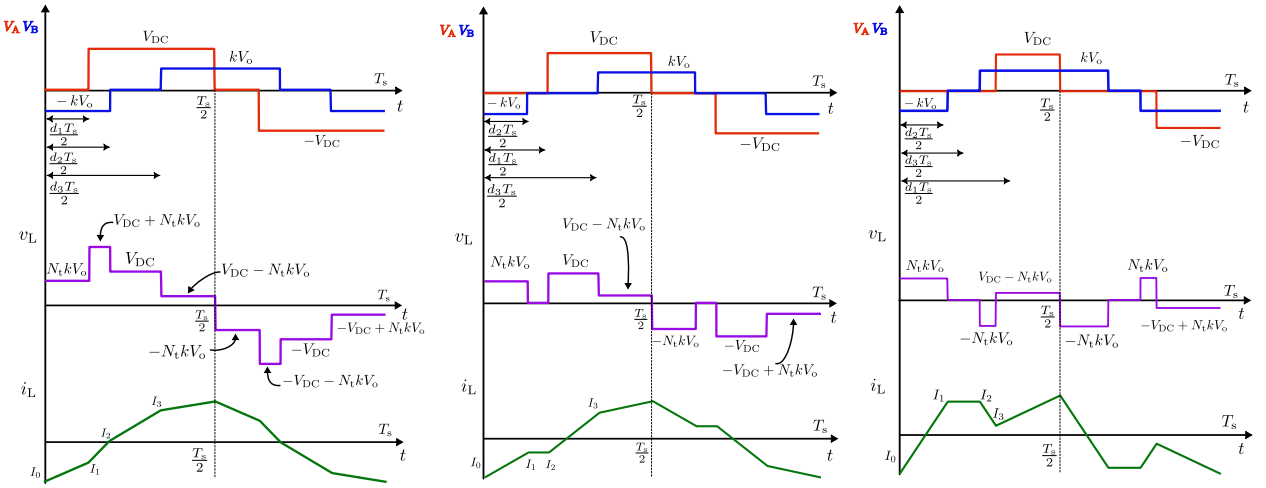

FIGURE 6. Modes of operation in the TPS modulation scheme. (a) Mode-I, ($d_1 \leq d_2 \leq d_3$). (b) Mode-II, ($d_2 \leq d_1 \leq d_3$). (c) Mode-III, ($d_2 \leq d_3 \leq d_1$).

TABLE 3. Operating Modes in TPS Modulation

Mode - I ($d_1 \leq d_2 \leq d_3$)		Mode - II ($d_2 \leq d_1 \leq d_3$)		Mode - III ($d_2 \leq d_3 \leq d_1$)	
$I_0 =$	$A(-k(d_2 + d_3 - 1) + d_1 - 1)$	$I_0 =$	$A(-k(d_2 + d_3 - 1) + d_1 - 1)$	$I_0 =$	$A(-k(d_2 + d_3 - 1) + d_1 - 1)$
$I_1 =$	$A(k(2d_1 - d_2 - d_3 + 1) + d_1 - 1)$	$I_1 =$	$A(k(d_2 - d_3 + 1) + d_1 - 1)$	$I_1 =$	$A(k(d_2 - d_3 + 1) + d_1 - 1)$
$I_2 =$	$A(k(d_2 - d_3 + 1) - d_1 + 2d_2 - 1)$	$I_2 =$	$A(k(d_2 - d_3 + 1) + d_1 - 1)$	$I_2 =$	$A(k(d_2 - d_3 + 1) + d_1 - 1)$
$I_3 =$	$A(k(d_2 - d_3 + 1) - d_1 + 2d_3 - 1)$	$I_3 =$	$A(k(d_2 - d_3 + 1) - d_1 + 2d_3 - 1)$	$I_3 =$	$A(k(d_2 - 2d_1 + d_3 + 1) + d_1 - 1)$
$P_o =$	$kAV_{DC}(-d_1(1 + d_1 - d_2 - d_3) - d_2(d_2 - 1) - d_3(d_3 - 1))$	$P_o =$	$kAV_{DC}(-d_1(1 + d_2 - d_3) + d_2 + d_3(1 - d_3)$	$P_o =$	$kAV_{DC}(1 - d_1)(d_2 - d_1 + d_3)$

Figs. 5 and 6 showcase the output voltages of both H-bridges V_A and V_B for DPS and TPS, respectively. Unlike the two-level waveforms in the case of SPS, as illustrated in Fig. 4, output voltages in DPS and TPS are three-level ac waveforms. The presence of the zero level helps reduce the area under the period during which the voltage undergoes zero crossing, while the current does not. This area contributes to the reactive power. TPS helps reduce this area significantly, followed by DPS, compared to SPS at lower operating powers when reactive power becomes more dominant, as will be evident in subsequent sections.

IV. CHOICE OF THE OPTIMIZATION SCHEME FOR DPS AND TPS

The selection of phase-shift ratios for the SPS scheme is relatively straightforward, as only one control variable exists. However, DPS and TPS modulation schemes contain more than one control variable. Therefore, there exist infinite possible combinations of d_1, d_2, and d_3 to achieve an operating power for a given operating mode. As a result, phase-shift ratios in the case of DPS and TPS need to be determined based on optimization objectives.

Kim et al. [50] have modified the DPS scheme by implementing various optimization strategies. Three different optimization strategies are considered: minimum reactive power, minimum peak current, and minimum RMS current. The efficiency of the converter has been compared over a wide voltage range for each of the optimization methods. It has been concluded that the peak current and RMS current optimization strategies performed the best. Similarly, Hou and Li [51] performed a comprehensive comparison of modulation and control strategies for the DAB converter. It has been concluded that the minimal current stress optimization and minimal RMS current optimization performed the best.

In this work, the determination of the phase-shift ratios for both DPS and TPS will be carried out based on the peak current optimization for electrolysis. Contrary to the approach reviewed in [51], this work employs a different approach to perform the peak current optimization for the process of electrolysis. The following assumptions have been made while conducting the optimization process.

1) The effects of dead time are neglected.
2) The parasitic effects of the circuit are neglected for the sake of simplicity.

To perform peak current optimization, this work uses the "fmincon" function in MATLAB to determine the phase-shift ratios for DPS and TPS schemes.

The minimum of a problem is specified by

$$\min_x f(x) \ni \begin{cases} c(x) \le 0 \\ c_{eq}(x) = 0 \\ A_{ineq} \cdot x \le b_{ineq} \\ A_{eq} \cdot x = b_{eq} \\ l \le x \le u \end{cases} \tag{10}$$

TABLE 4. Selection of K_x for the Modulation Schemes and Their Associated Modes Under Study

Modulation	K_0	K_1	K_2	K_3
DPS-I	−1	−1	−1	1
DPS-II	−1	−1	−1	1
DPS-III	−1	−1	1	1
DPS-IV	−1	−1	−1	1
TPS-I	−1	−1	1	1
TPS-II	−1	−1	−1	1
TPS-III	−1	1	1	1

where $f(x)$ is the objective function that needs to be minimized. $c(x)$ is the inequality cost function. $c_{eq}(x)$ is the equality cost function. A_{ineq} is the inequality constraint matrix. A_{eq} is the equality constraint matrix. b_{ineq} and b_{eq} are constant column matrices. l and u are the lower and upper bounds of x, respectively.

The objective function for the peak current during electrolysis, $i_{L(peak)}$ for a given mode in both DPS and TPS schemes, is given by

$$i_{L(peak)}(d,k) = \max(K_0 I_0, K_1 I_1, K_2 I_2, K_3 I_3). \tag{11}$$

As the reaction during electrolysis continues, I_0, which has been considered as the peak current with reference to Figs. 5 and 6, may not necessarily be the peak current for the entire operating region of the electrolyzer. The peak current value keeps shifting between I_0, I_1, I_2, and I_3. By using (11), this shift in the peak current is taken into account over the entire operating region of the electrolyzer and across all modes of operation under study. Furthermore, it simplifies the formulation process of the objective function. Table 4 provides values for K_x in (11) for each modulation scheme and its associated modes.

Using (10), the peak current optimization problem for DPS and TPS can be defined

$$\min_d i_{L(peak)}(d,k) \ni \begin{cases} P_o(d,k) = P_{stack} \\ A_{ineq} \cdot d \le b_{ineq} \\ d_{min} \le d \le d_{max}. \end{cases} \tag{12}$$

Table 5 provides the equality and inequality constraint matrices A_{ineq}, A_{eq}, b_{ineq}, and b_{eq} for DPS and TPS. These inequality matrices are constructed based on the constraints on the phase-shift ratios in each mode of DPS and TPS schemes, respectively.

The equality cost function for both DPS and TPS is given by

$$c_{eq}(d,k) = P_o(d,k) - P_{stack} = P_o(d,k) - v_{stack} i_{stack} \tag{13}$$

where P_o is the output power for various operating modes of DPS and TPS from Tables 2 and 3, respectively. P_{stack} is the target operating power that needs to be achieved based on the electrolyzer's characteristics, which can be obtained using (1)–(5). d is the phase-shift ratio matrix defined as $[d_1, d_2]$ for DPS, and $[d_1, d_2, d_3]$ for TPS. The lower and upper bounds

TABLE 5. Selection of Equality and Inequality Matrices for DPS and TPS Modulation

Modulation	A_{ineq}	A_{eq}	b_{ineq}	b_{eq}
DPS				
Mode-I	$\begin{bmatrix} 1 & -1 \\ 1 & 1 \end{bmatrix}$	0	$\begin{bmatrix} 0 & 1 \end{bmatrix}$	0
Mode-II	$\begin{bmatrix} -1 & 1 \\ 1 & 1 \end{bmatrix}$	0	$\begin{bmatrix} 0 & 1 \end{bmatrix}$	0
Mode-III	$\begin{bmatrix} 1 & -1 \\ -1 & -1 \end{bmatrix}$	0	$\begin{bmatrix} 0 & -1 \end{bmatrix}$	0
Mode-IV	$\begin{bmatrix} -1 & 1 \\ -1 & -1 \end{bmatrix}$	0	$\begin{bmatrix} 0 & -1 \end{bmatrix}$	0
TPS				
Mode-I	$\begin{bmatrix} -1 & -1 & 0 \\ 0 & 1 & -1 \end{bmatrix}$	0	0	0
Mode-II	$\begin{bmatrix} -1 & 1 & 0 \\ 1 & 0 & -1 \end{bmatrix}$	0	0	0
Mode-III	$\begin{bmatrix} 0 & 1 & -1 \\ -1 & 0 & 1 \end{bmatrix}$	0	0	0

TABLE 6. Considered DAB Converters for Electrolyzers

Parameters	1 kW	10 kW	100 kW
V_{DC}	500 V	1400 V	1400 V
V_{o}	70 V	70 V	100 V
N_{t}	7:1	20:1	14:1
L	580 μH	580 μH	50 μH
f_{sw}	20 kHz	20 kHz	20 kHz
C_{o}	210 μF	440 μF	6.3 mF

are defined by $d_{\min} = [0, 0]$ and $d_{\max} = [1, 1]$ for DPS, and $d_{\min} = [0, 0, 0]$ and $d_{\max} = [1, 1, 1]$ for TPS. Fig. 7 illustrates the optimization scheme.

V. COMPARISON OF MODULATION STRATEGIES

Based on the peak current optimization scheme for electrolysis presented in the previous section, an analysis is carried out by comparing the primary transformer peak currents during electrolysis. Three different electrolyzers are considered, each with a different power rating, i.e., 1, 10, and 100 kW, to additionally consider the effect of rated power. The phase-shift ratios for DPS and TPS schemes and, therefore, the resulting peak currents are determined based on the peak current optimization scheme described in the previous section. Electrolyzers are unique, nonlinear, low-voltage, and high-current loads. To illustrate this distinction, a similar analysis is conducted for a 500-V CV load (high-voltage and low-current load) with the same power rating.

Tables 6 and 7 showcase the DAB converter specifications for each case. The peak currents on the primary side of the transformer were measured for 19 operating power points: starting from 10% of rated power to the rated power.

Fig. 8 showcases a comparison of the transformer primary peak currents between DPS and SPS operation based on the analytical results of peak current optimization. For 1- and 10-kW electrolyzers, DPS Mode-I and SPS perform the best

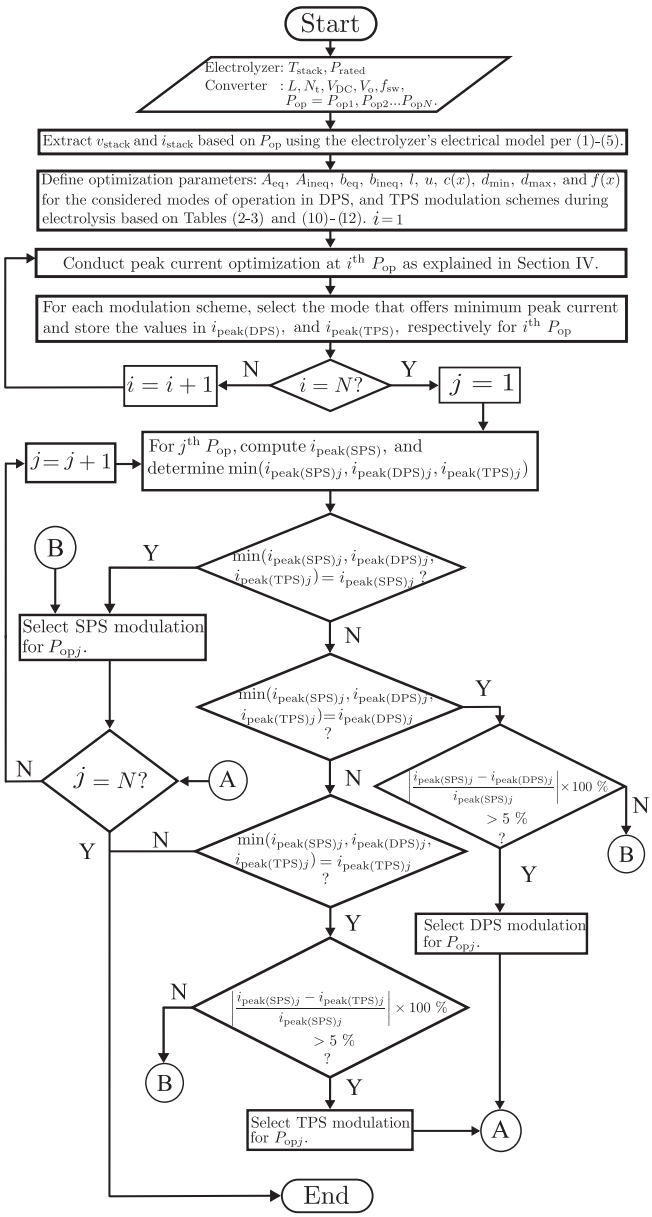

FIGURE 7. Flowchart to determine optimal modulation scheme during electrolysis for peak current optimization.

for both the loads, achieving minimum peak current until 0.4 and 5.5 kW, respectively. In both cases, DPS Mode-II offers the lowest peak current below 0.2 and 4 kW, respectively. However, in the case of the 100-kW power level, while DPS Mode-I/SPS performed the best overall for the CV load, this is not the case for the electrolyzer load. In the electrolyzer load, as the operating power begins to decrease, the peak currents for DPS Mode-I and SPS begin to increase. At an operating power close to 50 kW, a crossover is observed between the DPS Mode-I/SPS and DPS Mode-II. Below 50-kW power, DPS Mode-II performs the best by achieving the lowest peak current compared to DPS Mode-I, Mode-III, Mode-IV, and SPS.

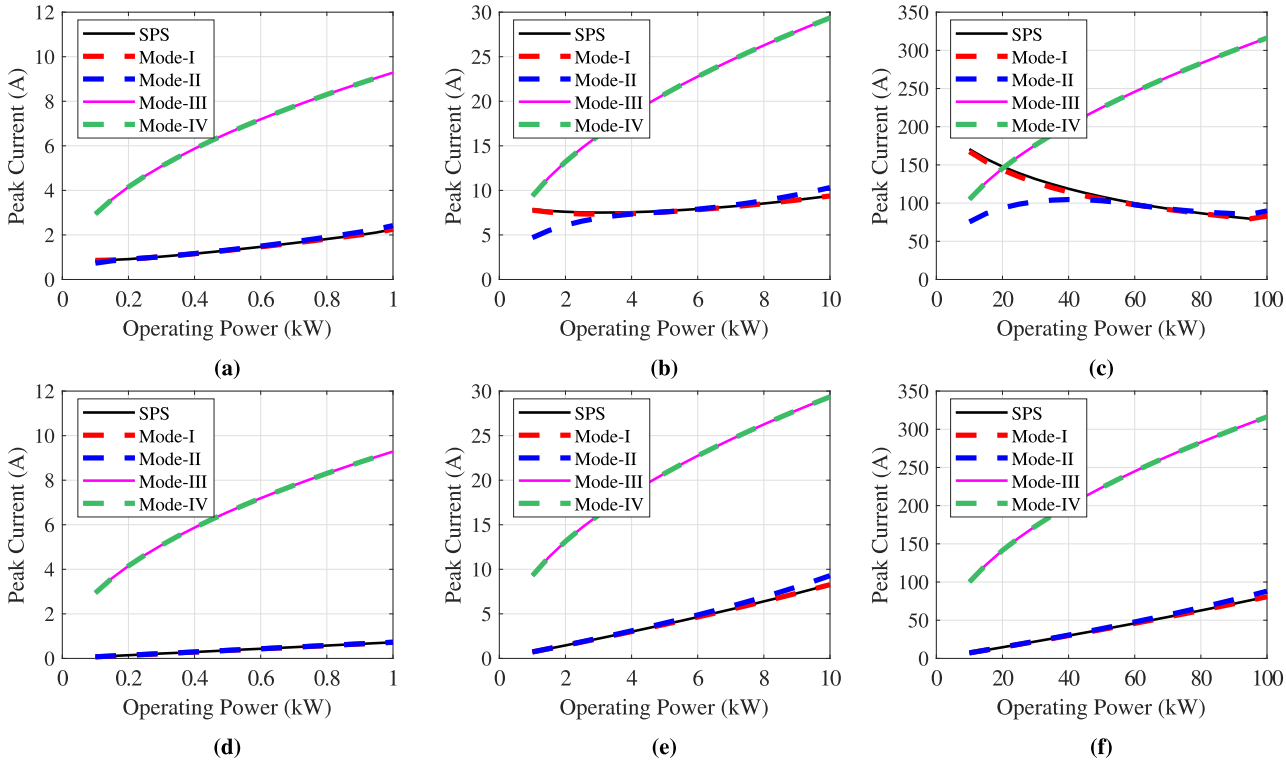

FIGURE 8. Comparison of studied DPS modes with conventional SPS operation for electrolyzer and CV loads. (a) 1-kW electrolyzer. (b) 10-kW electrolyzer. (c) 100-kW electrolyzer. (d) 1-kW CV load. (e) 10-kW CV load. (f) 100-kW CV load.

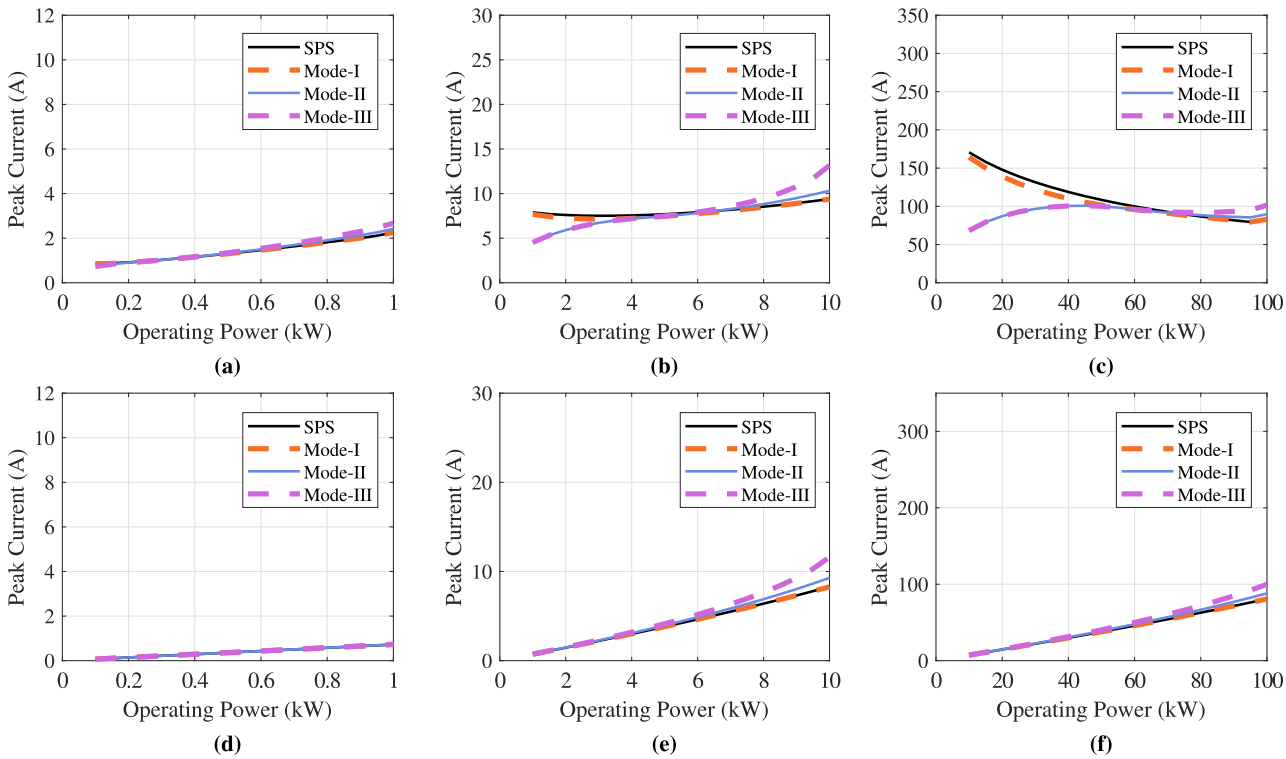

FIGURE 9. Comparison of studied TPS modes with conventional SPS operation for electrolyzer and CV loads. (a) 1-kW electrolyzer. (b) 10-kW electrolyzer. (c) 100-kW electrolyzer. (d) 1-kW CV load. (e) 10-kW CV load. (f) 100-kW CV load.

TABLE 7. Considered DAB Converters for CV Loads

Parameters	1 kW	10 kW	100 kW
V_{DC}	1400 V	1400 V	1400 V
V_o	500 V	500 V	500 V
N_t	2.8:1	2.8:1	2.8:1
L	580 μH	580 μH	50 μH
f_{sw}	20 kHz	20 kHz	20 kHz
C_o	210 μF	440 μF	6.3 mF

Similarly, Fig. 9 showcases the transformer primary peak currents based on the peak current optimization for the TPS modulation scheme, as well as during the SPS modulation scheme for electrolyzer and CV load for the considered test cases. For the test case of 1-kW CV load, SPS and all TPS modes of operation provide the same value of peak current for a given operating power. On the other hand, minor differences are observed during electrolysis. At the rated power, TPS Mode-I and SPS offer the lowest possible peak current, followed by TPS Mode-II, and finally TPS Mode-III. However, this trend begins to change as the operating power begins to decrease. As operating power approaches 400 W, the peak currents obtained with TPS Mode-III begin to decrease and, therefore, align with the peak currents of TPS Mode-I, TPS Mode-II, and SPS at 400 W. Below 200 W, the crossover finally occurs, wherein TPS Mode-II and TPS Mode-III provide the lowest possible peak current. For the case of 10- and 100-kW CV loads, the peak currents showcase a relatively similar trend. At the rated power, TPS Mode-I and SPS provide the lowest possible peak current. As the operating power decreases, the difference in performance between the TPS modes and SPS begins to decrease, too. However, this is not the case for the 10- and 100-kW electrolyzers. The difference in performance is clearly observed for these test cases in contrast to the 1-kW electrolyzer discussed previously. For both the electrolyzer loads, TPS Mode-I and SPS performed the best, followed by TPS Mode-II and TPS Mode-III. As the operating power decreased, a crossover was achieved at 6 kW, below which, TPS Mode-II and TPS Mode-III outperformed TPS Mode-I and SPS. A similar trend is observed for the 100-kW electrolyzer. The crossover occurs between 60 and 80 kW. TPS Mode-II and TPS Mode-III outperform TPS Mode-I and SPS by a significant margin.

Using Figs. 8(a)–(c) and 9(a)–(c), comparison of studied DPS modes and TPS modes is carried out from the context of peak current reduction with SPS modulation as a baseline. This comparison is illustrated in Figs. 10 and 11, where positive percentage values indicate improvement, while negative percentage values indicate worse performance. In DPS Mode-I, peak current reduction is nearly identical to SPS, with only a minor reduction of 3.62% at 0.35 p.u. for the 100-kW electrolyzer, as illustrated in Fig. 10(a). In contrast, DPS Modes II–IV underperform near rated power but achieve substantial improvements at lower operating points. At 0.1 p.u., DPS Mode-II reduces peak current by 55.83%, 40.52%, and 15.09% for the 100-, 10-, and 1-kW electrolyzers, respectively, as shown in Fig. 10(b). Mode-III and Mode-IV show similar behavior, with the 100-kW electrolyzer reaching 38.51% reduction at 0.1 p.u., as shown in Fig. 10(c)–(d).

In case of TPS modulation, TPS Mode-I resembled DPS Mode-I but delivered greater peak current reduction for the 100-kW case, achieving 7.41% reduction at 0.35 p.u., as illustrated in Fig. 11(a). TPS Modes II and III, while less effective near rated power, provide significant peak current reduction at low power levels. At 0.1 p.u., both modes achieved reductions of 60% (100 kW), 42.71% (10 kW), and 15.75% (1 kW), as shown in Fig. 11(b) and (c).

Each mode of operation in both DPS and TPS is optimized for the lowest possible peak current it can offer while strictly operating in that specific mode. However, additional steps need to be considered so that the best possible mode of operation among all three modulation schemes can be identified for optimal operation of the converter during electrolysis. The detailed steps, as illustrated in Fig. 7, showcase subsequent steps post optimization scheme in order to obtain an optimized operating trajectory for the converter during electrolysis by selecting the best possible mode of operation among the studied modulation schemes for N operating points.

The determination of an optimal modulation scheme mainly depends on evaluating the deviation between the peak current during SPS modulation and either the DPS or the TPS modulation scheme

$$\left| \frac{i_{peak(SPS)} - i_{peak(X)}}{i_{peak(SPS)}} \right| \times 100\% > \epsilon \tag{14}$$

where ϵ determines the deviation threshold. X in (14) can either be SPS, DPS, or TPS.

With reference to the flowchart illustrated in Fig. 7, the optimal operating trajectory of the converter during electrolysis is determined for the considered power levels, as illustrated in Fig. 12. Operation under the SPS scheme is used as the reference. To highlight the effect of the deviation threshold, ϵ, Fig. 12 presents the optimized trajectories of the DAB converter for 1-, 10-, and 100-kW electrolyzers at $\epsilon = 2\%$, $\epsilon = 5\%$, and $\epsilon = 10\%$ illustrated in Fig. 12(a)–(c), (d)–(f), and (g)–(i), respectively.

For a deviation threshold of $\epsilon = 2\%$, the preferred operation varies with electrolyzer size. In the case of a 1-kW electrolyzer, TPS Mode-III is selected up to 200 W, after which the converter transitions to SPS modulation for the remainder of the operating range, as shown in Fig. 12(a). In the case of a 10-kW electrolyzer, TPS Mode-III is used up to 4 kW, TPS Mode-I is selected between 4 and 6.5 kW, and SPS modulation is applied above 6.5 kW, as shown in Fig. 12(b). In the case of a 100-kW electrolyzer, TPS Mode-III is preferred up to 60 kW, TPS Mode-I between 60 and 75 kW, and SPS modulation beyond 75 kW, as shown in Fig. 12(c).

For a deviation threshold of $\epsilon = 5\%$, fewer transitions between modulation schemes are observed compared to $\epsilon = 2\%$, as shown in Fig. 12(d)–(f). In the case of 1-kW electrolyzer, SPS modulation is favored for most of the operating

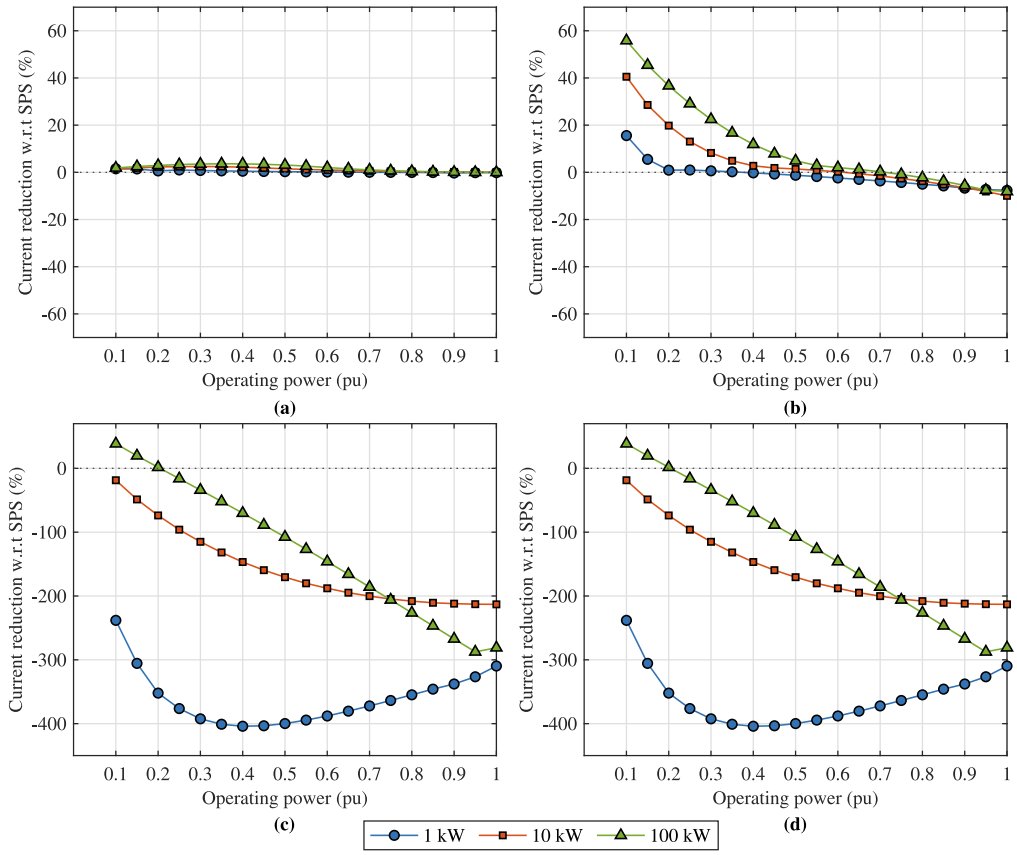

FIGURE 10. Comparison of studied DPS modes with conventional SPS operation from the context of peak current reduction during electrolysis: (a) DPS Mode-I, (b) DPS Mode-II, (c) DPS Mode-III, and (d) DPS Mode-IV.

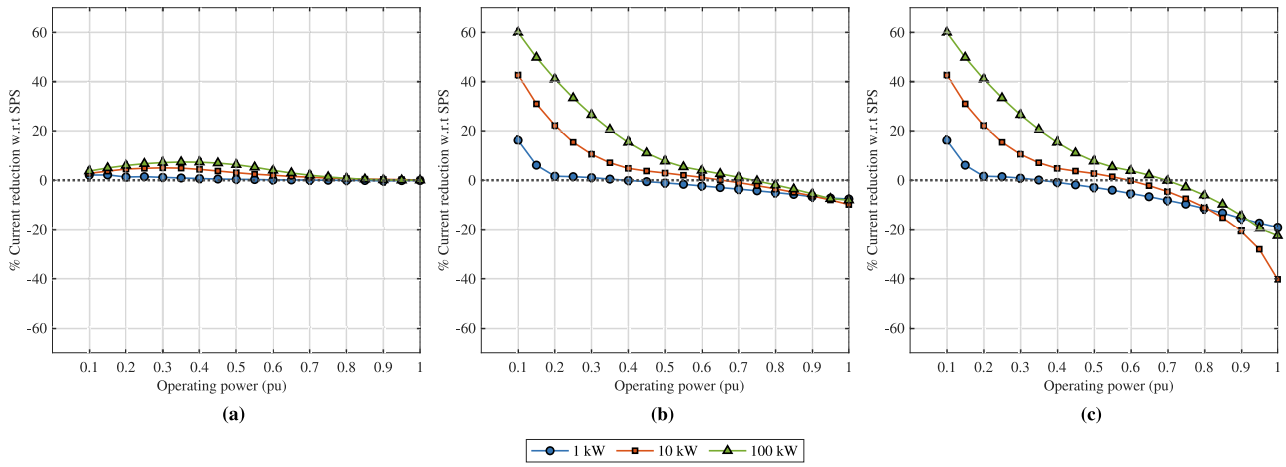

FIGURE 11. Comparison of studied TPS modes with conventional SPS operation from the context of peak current reduction during electrolysis: (a) TPS Mode-I, (b) TPS Mode-II, and (c) TPS Mode-III.

range, except below 200 W where TPS Mode-III is selected. In this region, a peak current reduction of up to 15.75% at 100 W is achieved, as shown in Fig. 12(d). In the case of a 10-kW electrolyzer, SPS modulation is preferred above 4 kW, while below this level, TPS Mode-III provides superior performance, yielding a peak current reduction of up to 42.71% at 1 kW, as shown in Fig. 12(e). Similarly, for the 100-kW electrolyzer, SPS modulation is selected above 60 kW, and TPS Mode-III is used below 60 kW, resulting in a peak current reduction of up to 60% at 10 kW, as shown in Fig. 12(f).

For a higher deviation threshold of $\epsilon = 10\%$, SPS modulation becomes dominant. In the 1-kW electrolyzer, TPS Mode-III is applied only up to 150 W, with SPS modulation covering the remainder of the range, as shown in Fig. 12(g). In

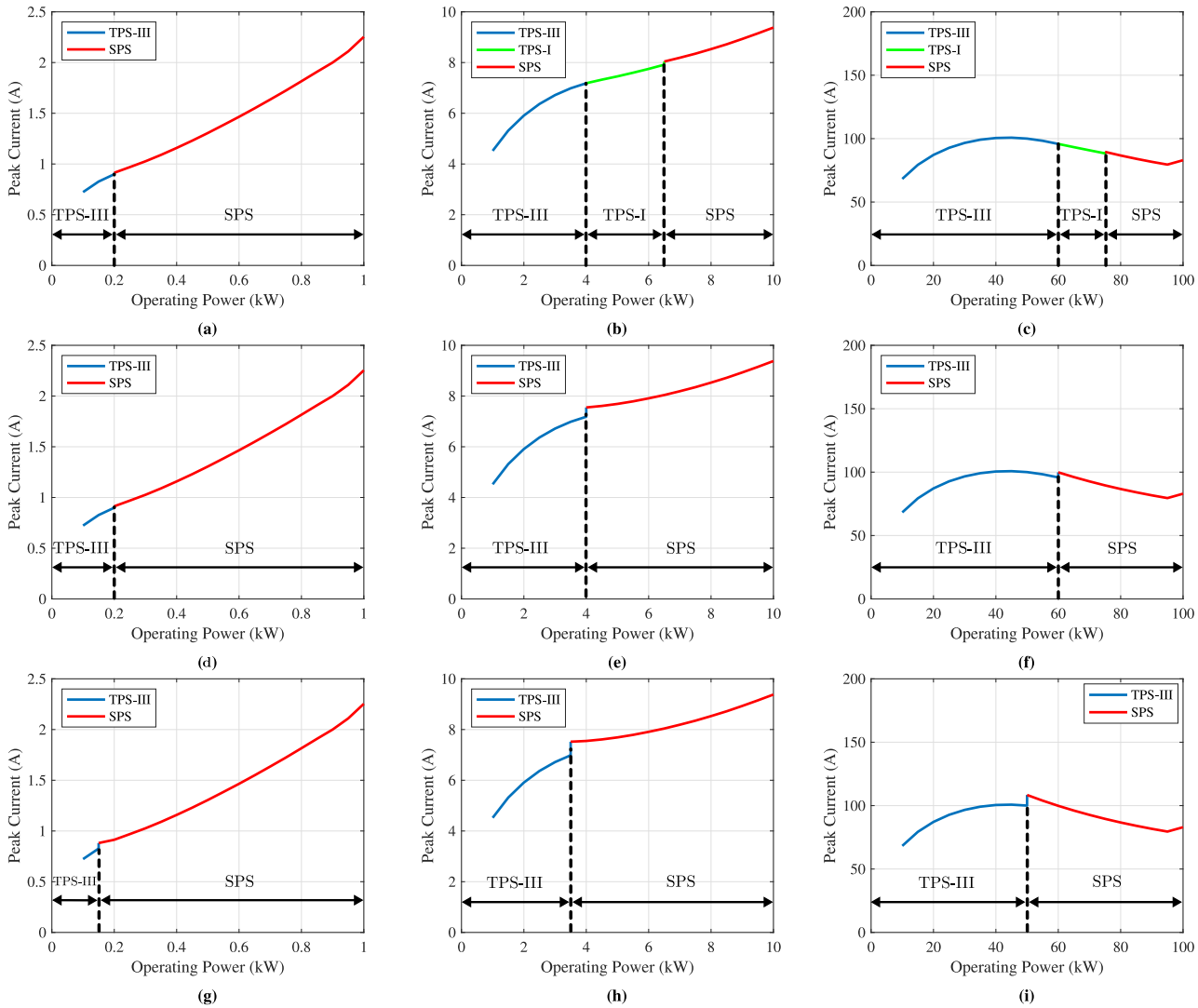

FIGURE 12. **Optimized operation for electrolysis based on deviation threshold: $\epsilon = 2\%$: (a) 1 kW, (b) 10 kW, and (c) 100 kW. $\epsilon = 5\%$: (d) 1 kW, (e) 10 kW, and (f) 100 kW. $\epsilon = 10\%$: (g) 1 kW, (h) 10 kW, and (i) 100 kW.**

the 10-kW case, TPS Mode-III is preferred below 3.5 kW and SPS above this point, as shown in Fig. 12(h). For the 100-kW electrolyzer, TPS Mode-III is selected up to 50 kW, while SPS modulation is used for higher power levels, as shown in Fig. 12(i).

The results in Fig. 12(a)–(i) show that a lower deviation threshold enables utilization of different modulation schemes and their associated modes. Conversely, a higher deviation threshold minimizes transitions, leading to operation primarily in the SPS scheme. Thus, $\epsilon = 5\%$ is considered in this work, which provides a balance between the number of transitions between modulation schemes and the minimization of peak current.

With reference to Fig. 12(d)–(f), another important observation is that the region where SPS modulation is preferred decreases as the rated electrolyzer power increases. For low-power electrolyzers, SPS provides the lowest peak current across most of the operating range, with TPS Mode-III applied only near the lower power limit, as shown in Fig. 12(d). However, for medium- and high-power electrolyzers, TPS becomes essential. The SPS scheme cannot minimize peak current effectively at lower operating points, which can result in increased reactive power within the system. In these cases, TPS outperforms both SPS and DPS, as demonstrated in Fig. 12(e)–(f).

VI. SIMULATION AND EXPERIMENTAL RESULTS

Fig. 13 showcases the experimental setup for this work. A 1-kW 20-kHz DAB prototype is designed and controlled in open loop using PLECS RT-Box 2 by implementing the modulation logic within PLECS. Based on the identified optimal operating trajectory, the phase-shift ratios (d_1, d_2, and d_3) are calculated offline and stored in a lookup table. The Infineon AIMZH120R020M1T silicon carbide MOSFETs are chosen as semiconductor switches in this prototype. Two bidirectional programmable dc power supplies are used. One of them is

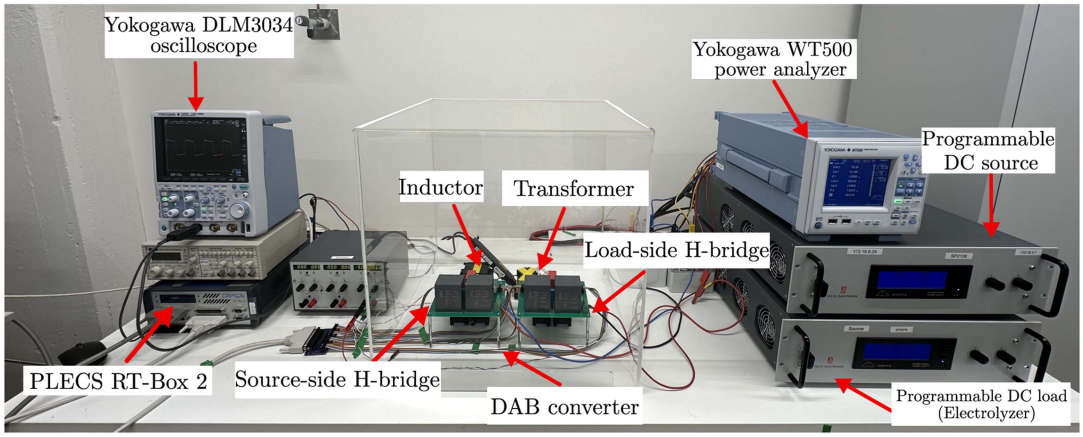

FIGURE 13. Experimental setup.

TABLE 8. Comparison of Simulation and Experimental Results Based on the Identified Optimized Trajectory ($\epsilon = 5\%$) for the 1-kW Prototype

Operating Power (kW)	Selected Mode	Simulation (A)	Experiment (A)
0.1	TPS-III	0.74	0.73
0.2	SPS	0.93	0.89
0.3	SPS	1.03	1.01
0.4	SPS	1.16	1.13
0.5	SPS	1.30	1.28
0.6	SPS	1.46	1.47
0.7	SPS	1.63	1.61
0.8	SPS	1.81	1.96
0.9	SPS	2.00	2.20
1	SPS	2.28	2.60

TABLE 9. Comparison of the Optimization Results With the Simulation Results Based on the Identified Optimized Trajectory ($\epsilon = 5\%$) for the 10-kW System

Operating Power (kW)	Selected Mode	Calculated optimized current (A)	Simulation (A)
1	TPS-III	4.60	4.67
2	TPS-III	5.80	5.82
3	TPS-III	6.63	6.53
4	SPS	7.44	7.33
5	SPS	7.57	7.45
6	SPS	7.77	7.83
7	SPS	8.04	8.09
8	SPS	8.38	8.40
9	SPS	8.77	8.79
10	SPS	9.22	9.23

TABLE 10. Comparison of the Optimization Results With the Simulation Results Based on the Identified Optimized Trajectory ($\epsilon = 5\%$) for the 100-kW System

Operating Power (kW)	Selected Mode	Calculated optimized current (A)	Simulation (A)
10	TPS-III	68.25	68.56
20	TPS-III	87.16	87.46
30	TPS-III	96.64	96.73
40	TPS-III	100.50	100.3
50	TPS-III	100.03	99.54
60	SPS	99.84	99.46
70	SPS	92.70	92.2
80	SPS	86.70	86.09
90	SPS	81.70	80.96
100	SPS	83.0	84.16

programmed as a dc source and set at 500 V, while the other is configured as a dc load that follows the electrical characteristics of the 1-kW electrolyzer. The efficiency measurement has been carried out with the help of a Yokogawa WT500 power analyzer. The peak value of the primary-side transformer current is measured using a Yokogawa DLM3034 oscilloscope.

The prototype is operated to follow along the optimal operation curve, as shown in Fig. 12(a). On the other hand, in order to validate the 10- and 100-kW cases, equivalent Simulink models are made to operate along their respective optimal operation curves. Table 8 provides a comparison of peak currents measured from the experimental setup against the simulation model operating on the optimized phase-shift ratios for the 1-kW system, and Fig. 14 showcases the primary transformer currents obtained from the prototype. On the other hand, Tables 9 and 10 provide a comparison between the peak currents of simulation results against the value of the objective function of the optimization problem for the 10- and 100-kW systems, respectively. Figs. 15 and 16 showcase the primary transformer currents for the 10- and 100-kW systems, respectively. The phase-shift ratios determined by the optimization scheme correctly result in the expected primary peak transformer current during electrolysis for the 1-kW case. On the other hand, simulation results for the 10- and 100-kW cases are in accordance with the peak current values obtained through the objective function of the optimization problem, showcasing that the proposed optimized operation for the converter during electrolysis effectively helps minimize the peak transformer current at lower operating power points during electrolysis.

Fig. 17 presents the measured efficiencies of the 1-kW experimental prototype operating under SPS, DPS, and TPS modulation schemes during electrolysis. At the rated power of 1 kW, all three schemes exhibit nearly identical efficiencies, with SPS at 96.20%, DPS at 96.17%, and TPS at 96.36%. This convergence occurs because, at rated power, DPS and TPS

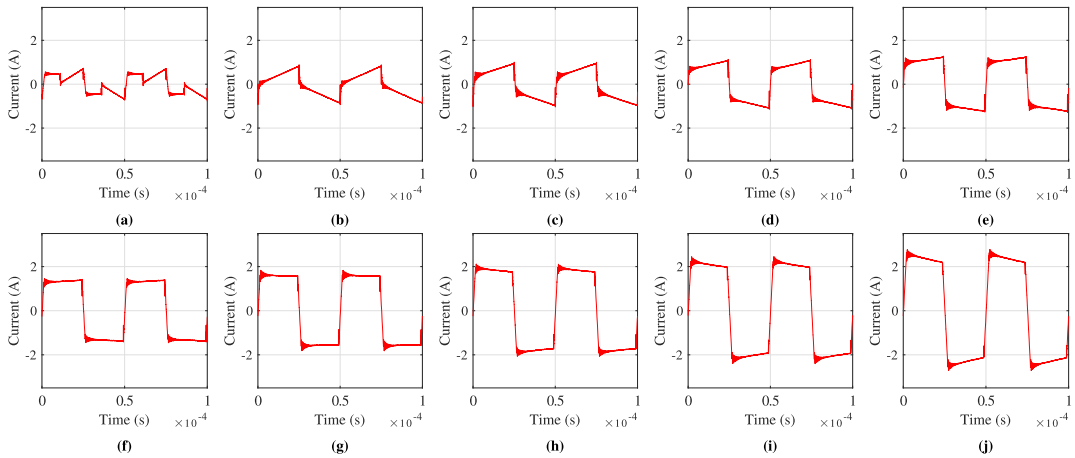

FIGURE 14. Experimental results of primary transformer current based on the identified optimized trajectory ($\epsilon = 5\%$): TPS-III in (a) 100 W, SPS in (b) 200 W, (c) 300 W, (d) 400 W, (e) 500 W, (f) 600 W, (g) 700 W, (h) 800 W, (i) 900 W, and (j) 1 kW.

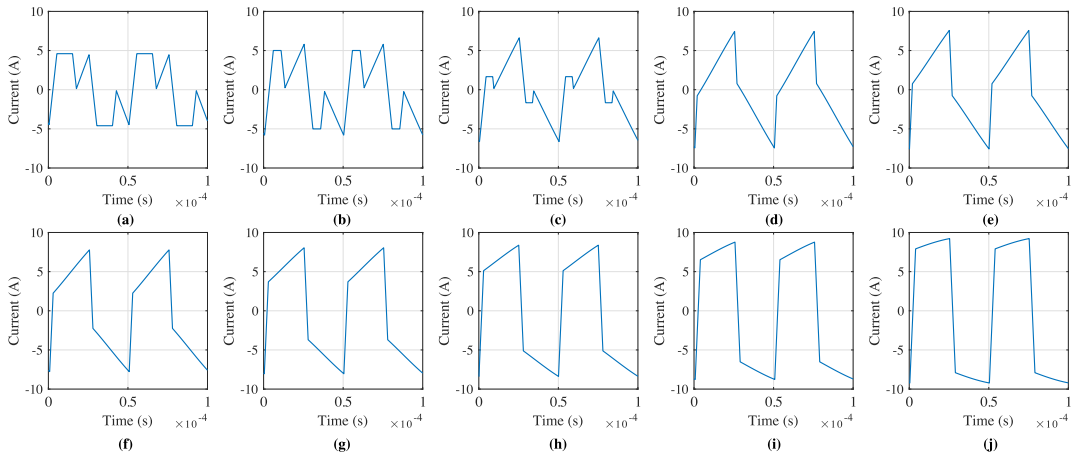

FIGURE 15. Simulation results of primary transformer current based on the identified optimized trajectory ($\epsilon = 5\%$): TPS-III in (a) 1 kW, (b) 2 kW, (c) 3 kW, SPS in (d) 4 kW, (e) 5 kW, (f) 6 kW, (g) 7 kW, (h) 8 kW, (i) 9 kW, and (j) 10 kW.

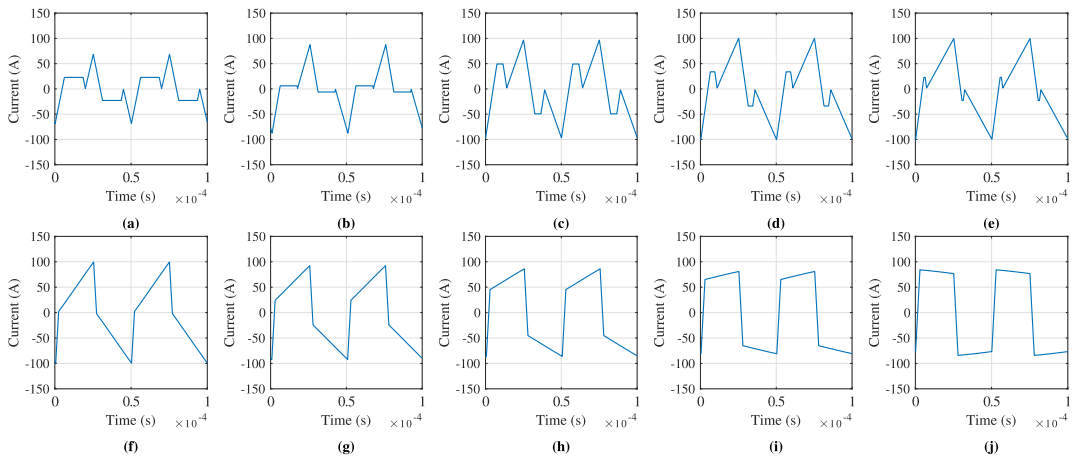

FIGURE 16. Simulation results of primary transformer current based on the identified optimized trajectory ($\epsilon = 5\%$): TPS-III in (a) 10 kW, (b) 20 kW, (c) 30 kW, (d) 40 kW, (e) 50 kW, SPS in (f) 60 kW, (g) 70 kW, (h) 80 kW, (i) 90 kW, and (j) 100 kW.

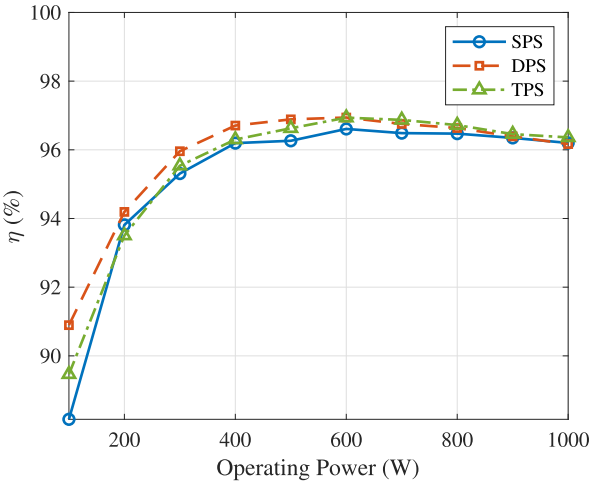

FIGURE 17. Measured efficiency of the 1-kW prototype in SPS, DPS, and TPS modes with an emulated 1-kW electrolyzer load.

effectively operate in a manner similar to SPS, as described in Section III-C. As the operating power decreases, the efficiency of SPS begins to drop, while DPS and TPS maintain a similar trend and even show slight improvements up to 600 W. Below 600 W, TPS efficiency gradually declines and falls slightly below that of DPS. At 100 W, DPS demonstrates the highest efficiency at 90.89%, followed by TPS at 89.46%, and SPS at 88.15%. While the proposed peak current optimization enables TPS to achieve the lowest peak current at low power, it also results in a slightly higher RMS current compared to DPS. As a result, DPS delivers marginally higher efficiency due to its lower RMS current despite the slightly higher peak current as compared to TPS, as shown in Fig. 17.

VII. CONCLUSION

This article has investigated state-of-the-art modulation schemes for the DAB converter with a focus on electrolysis applications. Due to their nonlinear, low-voltage, and high-current characteristics, electrolyzers pose distinct challenges compared to conventional CV loads. A comparative analysis across SPS, DPS, and TPS modulation schemes using peak primary transformer current as the evaluation metric has been conducted at three power levels: 1, 10, and 100 kW. To achieve this, a peak current optimization method based on MATLAB's fmincon function has been developed to determine optimal phase-shift ratios for DPS and TPS schemes. The results revealed that electrolyzers exhibit fundamentally different behavior than CV loads under the same operating conditions, highlighting the need to study modulation strategies for electrolysis.

Extending the optimization scheme, optimized operating trajectories for the DAB converter have been identified for each power level. While SPS remains the most effective for low-power electrolyzers, it proves suboptimal at medium to high power due to increased circulating currents and reactive power—issues that can be significantly mitigated with DPS and TPS schemes.

The proposed optimization framework has been validated through experiments using a 1-kW 20-kHz prototype and simulations for 10- and 100-kW systems. The optimized trajectories resulted in peak current reductions of up to 15.75% at 100 W for the 1-kW system, 42.71% at 1 kW for the 10-kW system, and 60% at 10 kW for the 100-kW system, compared to conventional SPS operation.

REFERENCES

[1] M. K. Abbas et al., "Techno-economic analysis for clean hydrogen production using solar energy under varied climate conditions," *Int. J. Hydrogen Energy*, vol. 48, no. 8, pp. 2929–2948, 2023.
[2] S. Qazi, A. Abdelhakim, T. B. Soeiro, Q. Xu, S. Bosga, and F. Canales, "Electrified hydrogen systems: An overview," *IEEE Ind. Electron. Mag.*, 2025.
[3] L. Gracia, P. Casero, C. Bourasseau, and A. Chabert, "Use of hydrogen in off-grid locations, a techno-economic assessment," *Energies*, vol. 11, no. 11, 2018, Art. no. 3141.
[4] Q. Hassan, I. S. Abdulrahman, H. M. Salman, O. T. Olapade, and M. Jaszczur, "Techno-economic assessment of green hydrogen production by an off-grid photovoltaic energy system," *Energies*, vol. 16, no. 2, 2023, Art. no. 744.
[5] D. Guilbert, S. M. Collura, and A. Scipioni, "DC/DC converter topologies for electrolyzers: State-of-the-art and remaining key issues," *Int. J. Hydrogen Energy*, vol. 42, no. 38, pp. 23966–23985, 2017.
[6] M. B. El Kattel et al., "Overview of main electrolyzer technologies and power electronic converter topologies for enabling hydrogen production through water electrolysis," *Int. J. Circuit Theory Appl.*, vol. 53, no. 6, pp. 3684–3718, 2024.
[7] R. S. Deshmukh, A. Shekhar, and P. Bauer, "Adaptive modularity for power electronics based electrolysis systems for green hydrogen," in *Proc. IEEE 20th Int. Power Electron. Motion Control Conf.*, 2022, pp. 508–515.
[8] N. Hou and Y. W. Li, "A tunable power sharing control scheme for the output-series DAB DC–DC system with independent or common input terminals," *IEEE Trans. Power Electron.*, vol. 34, no. 10, pp. 9386–9391, Oct. 2019.
[9] B. Zhao, Q. Song, J. Li, Y. Wang, and W. Liu, "High-frequency-link modulation methodology of DC–DC transformer based on modular multilevel converter for HVDC application: Comprehensive analysis and experimental verification," *IEEE Trans. Power Electron.*, vol. 32, no. 5, pp. 3413–3424, May 2017.
[10] F. D. Freijedo, E. Rodriguez-Diaz, and D. Dujic, "Stable and passive high-power dual active bridge converters interfacing MVDC grids," *IEEE Trans. Ind. Electron.*, vol. 65, no. 12, pp. 9561–9570, Dec. 2018.
[11] P. Nayak, S. Mandal, Y. Gupta, A. Shukla, and S. Doolla, "Improving the efficiency of the DAB converter of an on-board EV charger using different modulation techniques," in *Proc. IEEE Int. Conf. Power Electron. Drives Energy Syst.*, 2020, pp. 1–6.
[12] A. V. Mirtchev and E. C. Tatakis, "Design methodology based on dual control of a resonant dual active bridge converter for electric vehicle battery charging," *IEEE Trans. Veh. Technol.*, vol. 71, no. 3, pp. 2691–2705, Mar. 2022.
[13] D. Chen, J. Deng, W. Wang, and Z. Wang, "A dual-transformer-based hybrid dual active bridge converter for plug-in electric vehicle charging to cope with wide load voltages," *IEEE Trans. Ind. Electron.*, vol. 70, no. 2, pp. 1444–1454, Feb. 2023.
[14] Y. Xuan, X. Yang, W. Chen, T. Liu, and X. Hao, "A three-level dual-active-bridge converter with blocking capacitors for bidirectional electric vehicle charger," *IEEE Access*, vol. 7, pp. 173838–173847, 2019.
[15] H. V. Nguyen, D.-D. To, and D.-C. Lee, "Onboard battery chargers for plug-in electric vehicles with dual functional circuit for low-voltage battery charging and active power decoupling," *IEEE Access*, vol. 6, pp. 70212–70222, 2018.
[16] F. Krismer and J. W. Kolar, "Efficiency-optimized high-current dual active bridge converter for automotive applications," *IEEE Trans. Ind. Electron.*, vol. 59, no. 7, pp. 2745–2760, Jul. 2012.

[17] J. Shi, W. Gou, H. Yuan, T. Zhao, and A. Q. Huang, "Research on voltage and power balance control for cascaded modular solid-state transformer," *IEEE Trans. Power Electron.*, vol. 26, no. 4, pp. 1154–1166, Apr. 2011.
[18] T. Zhao, G. Wang, S. Bhattacharya, and A. Q. Huang, "Voltage and power balance control for a cascaded H-bridge converter-based solid-state transformer," *IEEE Trans. Power Electron.*, vol. 28, no. 4, pp. 1523–1532, Apr. 2013.
[19] X. She, A. Q. Huang, and X. Ni, "Current sensorless power balance strategy for DC/DC converters in a cascaded multilevel converter based solid state transformer," *IEEE Trans. Power Electron.*, vol. 29, no. 1, pp. 17–22, Jan. 2014.
[20] S. Falcones, R. Ayyanar, and X. Mao, "A DC–DC multiport-converter-based solid-state transformer integrating distributed generation and storage," *IEEE Trans. Power Electron.*, vol. 28, no. 5, pp. 2192–2203, May 2013.
[21] R. Naayagi, A. Forsyth, and R. Shuttleworth, "Bidirectional control of a dual active bridge DC–DC converter for aerospace applications," *IET Power Electron.*, vol. 5, no. 7, pp. 1104–1118, 2012.
[22] G. Buticchi, D. Barater, L. F. Costa, and M. Liserre, "A PV-inspired low-common-mode dual-active-bridge converter for aerospace applications," *IEEE Trans. Power Electron.*, vol. 33, no. 12, pp. 10467–10477, Dec. 2018.
[23] N. M. L. Tan, T. Abe, and H. Akagi, "Design and performance of a bidirectional isolated DC–DC converter for a battery energy storage system," *IEEE Trans. Power Electron.*, vol. 27, no. 3, pp. 1237–1248, Mar. 2012.
[24] F. Xue, R. Yu, and A. Q. Huang, "A 98.3% efficient GAN isolated bidirectional DC–DC converter for DC microgrid energy storage systemapplications," *IEEE Trans. Ind. Electron.*, vol. 64, no. 11, pp. 9094–9103, Nov. 2017.
[25] V. Karthikeyan and R. Gupta, "Multiple-input configuration of isolated bidirectional DC–DC converter for power flow control in combinational battery storage," *IEEE Trans. Ind. Informat.*, vol. 14, no. 1, pp. 2–11, Jan. 2018.
[26] D.-D. Nguyen, K. Yukitta, A. Katou, and S. Yoshida, "A comparison study of modulation methods for three-phase dual-active-bridge converters in battery charging applications," in *Proc. IEEE 12th Energy Convers. Congr. Expo.*, 2021, pp. 1033–1038.
[27] L. Feng, Z. Zhang, X. Fu, and X. Guo, "Analysis and comparison of partial power converters based on dual active bridge and isolated full-bridge boost in hydrogen production system," in *Proc. IEEE 2nd Int. Power Electron. Appl. Symp.*, 2023, pp. 2532–2537.
[28] A. Ganjavi, S. A. Gorji, A. Hakemi, A. Moradi, and D. Sera, "Design and implementation of an SiC-based 48 V-380 V dual active bridge DC-DC converter for batteries employed in green hydrogen microgrids," in *Proc. IEEE 7th Southern Power Electron. Conf.*, 2022, pp. 1–6.
[29] N. Fritz, T. Sechel, P. Kowalewski, and R. W. De Doncker, "Optimizing current-fed, GAN-based DC-DC converters for electrolysis applications," in *Proc. 11th Int. Conf. Power Electron. ECCE Asia*, 2023, pp. 2843–2850.
[30] R. S. Deshmukh, G. Rituraj, N. Lock, H. Vahedi, A. Shekhar, and P. Bauer, "Implementation of real-time digital twin of dual active bridge converter in electrolyzer applications," in *Proc. 49th Annu. Conf. IEEE Ind. Electron. Soc.*, 2023, pp. 1–6.
[31] R. S. Deshmukh, G. Rituraj, H. Vahedi, A. Shekhar, and P. Bauer, "Impact of electrolyzer on the operation of a dual active bridge converter," in *Proc. 49th Annu. Conf. IEEE Ind. Electron. Soc.*, 2023, pp. 1–6.
[32] R. S. Deshmukh, G. Rituraj, P. Bauer, and H. Vahedi, "Real-time digital twin implementation of power electronics-based hydrogen production system," *Energy Rep.*, vol. 13, pp. 5006–5015, 2025.
[33] Ø. Ulleberg, "Modeling of advanced alkaline electrolyzers: A system simulation approach," *Int. J. Hydrogen Energy*, vol. 28, no. 1, pp. 21–33, 2003.
[34] D. Falcão and A. Pinto, "A review on PEM electrolyzer modelling: Guidelines for beginners," *J. Clean. Prod.*, vol. 261, 2020, Art. no. 121184.
[35] A. Ursúa and P. Sanchis, "Static–dynamic modelling of the electrical behaviour of a commercial advanced alkaline water electrolyser," *Int. J. Hydrogen Energy*, vol. 37, no. 24, pp. 18598–18614, 2012.
[36] N. Gallandat, K. Romanowicz, and A. Züttel, "An analytical model for the electrolyser performance derived from materials parameters," *J. Power Energy Eng.*, vol. 5, no. 10, pp. 34–49, 2017.
[37] D. A. Aikens, "Electrochemical methods, fundamentals and applications," *J. Chem. Educ.*, vol. 60, no. 1, p. A25, 1983, doi: 10.1021/ed060pA25.1.
[38] S. Inoue and H. Akagi, "A bidirectional isolated DC–DC converter as a core circuit of the next-generation medium-voltage power conversion system," *IEEE Trans. Power Electron.*, vol. 22, no. 2, pp. 535–542, Mar. 2007.
[39] S. Inoue and H. Akagi, "A bidirectional DC–DC converter for an energy storage system with galvanic isolation," *IEEE Trans. Power Electron.*, vol. 22, no. 6, pp. 2299–2306, Nov. 2007.
[40] R. W. De Doncker, D. M. Divan, and M. H. Kheraluwala, "A three-phase soft-switched high-power-density DC/DC converter for high-power applications," *IEEE Trans. Ind. Appl.*, vol. 27, no. 1, pp. 63–73, Jan./Feb. 1991.
[41] M. Kheraluwala, R. W. Gascoigne, D. M. Divan, and E. D. Baumann, "Performance characterization of a high-power dual active bridge DC-to-DC converter," *IEEE Trans. Ind. Appl.*, vol. 28, no. 6, pp. 1294–1301, Nov./Dec. 1992.
[42] B. Zhao, Q. Song, W. Liu, and Y. Sun, "Overview of dual-active-bridge isolated bidirectional DC–DC converter for high-frequency-link power-conversion system," *IEEE Trans. Power Electron.*, vol. 29, no. 8, pp. 4091–4106, Aug. 2014.
[43] A. K. Jain and R. Ayyanar, "PWM control of dual active bridge: Comprehensive analysis and experimental verification," *IEEE Trans. Power Electron.*, vol. 26, no. 4, pp. 1215–1227, Apr. 2011.
[44] H. Bai and C. Mi, "Eliminate reactive power and increase system efficiency of isolated bidirectional dual-active-bridge DC–DC converters using novel dual-phase-shift control," *IEEE Trans. Power Electron.*, vol. 23, no. 6, pp. 2905–2914, Nov. 2008.
[45] H. Bai, Z. Nie, and C. C. Mi, "Experimental comparison of traditional phase-shift, dual-phase-shift, and model-based control of isolated bidirectional DC–DC converters," *IEEE Trans. Power Electron.*, vol. 25, no. 6, pp. 1444–1449, Jun. 2010.
[46] B. Zhao, Q. Song, and W. Liu, "Power characterization of isolated bidirectional dual-active-bridge DC–DC converter with dual-phase-shift control," *IEEE Trans. Power Electron.*, vol. 27, no. 9, pp. 4172–4176, Sep. 2012.
[47] X. Liu et al., "Novel dual-phase-shift control with bidirectional inner phase shifts for a dual-active-bridge converter having low surge current and stable power control," *IEEE Trans. Power Electron.*, vol. 32, no. 5, pp. 4095–4106, May 2017.
[48] F. Krismer and J. W. Kolar, "Accurate small-signal model for the digital control of an automotive bidirectional dual active bridge," *IEEE Trans. Power Electron.*, vol. 24, no. 12, pp. 2756–2768, Dec. 2009.
[49] F. Krismer and J. W. Kolar, "Closed form solution for minimum conduction loss modulation of DAB converters," *IEEE Trans. Power Electron.*, vol. 27, no. 1, pp. 174–188, Jan. 2012.
[50] M. Kim, M. Rosekeit, S.-K. Sul, and R. W. De Doncker, "A dual-phase-shift control strategy for dual-active-bridge DC-DC converter in wide voltage range," in *Proc. 8th Int. Conf. Power Electron. ECCE Asia*, 2011, pp. 364–371.
[51] N. Hou and Y. W. Li, "Overview and comparison of modulation and control strategies for a nonresonant single-phase dual-active-bridge DC–DC converter," *IEEE Trans. Power Electron.*, vol. 35, no. 3, pp. 3148–3172, Mar. 2020.

ROHAN SHAILESH DESHMUKH (Graduate Student Member, IEEE) received the B.E. degree in electrical engineering from the Babaria Institute of Technology, Vadodara, India, in 2018, and the M.Sc. degree in electrical power engineering in 2021 from the Delft University of Technology, Delft, The Netherlands, where he is currently working toward the Ph.D. degree in electrical engineering with the DC Systems, Energy Conversion and Storage Research Group.

His research interests include designing, modeling, and controlling power electronics converters for high-power electrolysis systems.

Mr. Deshmukh received the Student and Young Professionals Paper Assistance Award by the IEEE Industrial Electronics Society in 2023.

GAUTAM RITURAJ (Member, IEEE) received the B.Tech. degree in electrical engineering from Uttar Pradesh Technical University, Lucknow, India, in 2012, and the Ph.D. degree in electrical engineering from the Indian Institute of Technology Guwahati, Guwahati, India, in 2021.

From 2021 to 2025, he was a Postdoctoral Researcher with the Delft University of Technology (TU Delft), Delft, The Netherlands, pursuing his research on off-grid EV charging, stand-alone microgrid design and optimization, hybrid energy storage integration, and electrolyzer systems. He is currently a Technical Staff Member with the ESP Lab, DCE&S Group, Department of Electrical Sustainable Energy, TU Delft. He holds one Indian patent. His current research interests include off-grid electric vehicle charging systems, electrolyzer systems, dc–dc converters, energy storage integration, analysis and design of wireless power transfer systems, coil design and modeling, and developing power electronic circuits for EV charging.

Dr. Rituraj is a recipient of the Gandhian Young Technological Innovation Appreciation 2021 for his doctoral work. His paper was recognized as a featured article in IEEE OPEN JOURNAL OF THE INDUSTRIAL ELECTRONICS SOCIETY in 2023.

PAVOL BAUER (Senior Member, IEEE) received the master's degree in electrical engineering from the Technical University of Kosice, Kosice, Slovakia, in 1985, and the Ph.D. degree in electrical engineering from the Delft University of Technology, Delft, The Netherlands, in 1995.

From 2002 to 2003, he was with KEMA (DNVGL), Arnhem, The Netherlands, on different projects related to power electronics applications in power systems. He is currently a Full Professor with the Department of Electrical Sustainable Energy, Delft University of Technology, and the Head of DC Systems, Energy Conversion, and Storage Group. He is also a Professor with the Brno University of Technology, Brno, Czech Republic, and an Honorary Professor with Politehnica University Timişoara, Timişoara, Romania. He has authored or coauthored more than 120 journal articles and 500 conference papers in his field. He is an author or coauthor of eight books, holds seven international patents, and has organized several tutorials at international conferences. He has worked on many projects for the industry concerning wind and wave energy, power electronic applications for power systems, such as Smart-trafo, HVdc systems, projects for smart cities such as photovoltaic (PV) charging of electric vehicles, PV and storage integration, and contactless charging. He participated in several Leonardo da Vinci and H2020, and Electric Mobility Europe EU projects as a Project Partner (ELINA, INETELE, E-Pragmatic, Micact, Trolley 2.0, OSCD, P2P, and Progressus) and a Coordinator (PEMCWebLab.com-Edipe, SustEner, and Eranet DCMICRO).

Dr. Bauer is the Former Chairperson of the Benelux IEEE Joint Industry Applications Society, Power Electronics and Power Engineering Society Chapter, and the Power Electronics and Motion Control Council. He is a Member of the Executive Committee of the European Power Electronics Association, and also a Member of the International Steering Committee at numerous conferences.

HANI VAHEDI (Senior Member, IEEE) received the Ph.D. (Hons.) degree in electrical engineering from the École de Technologie Superieure (ÉTS), University of Quebec, Montreal, QC, Canada, in 2016.

He has authored or coauthored more than 60 technical papers in IEEE conferences and Transactions. He also authored or coauthored a book on Springer Nature and a book chapter in Elsevier. He is the inventor of the PUC5 converter, holds multiple US/world patents, and transferred that technology to the industry, where he developed the first bidirectional electric vehicle dc charger based on his invention. After seven years of experience in industry as a Power Electronics Designer and Chief Scientific Officer, he joined the Delft University of Technology, Delft, The Netherlands, where he is currently an Assistant Professor with the DCE&S Group, working toward the electrification of industrial processes for clean energy transition. His research interests include multilevel converter topologies, control and modulation techniques, and their applications in the electrification of industrial processes and clean energy transition, such as smart grids, renewable energy conversion, electric vehicle chargers, green hydrogen production (electrolyzers), and fuel cell systems.

Dr. Vahedi was the recipient of the Best Ph.D. Thesis Award from ÉTS for the academic year of 2016 and 2017. He is an Active Member of the IEEE Industrial Electronics Society (IES) and its Student and Young Professionals (S&YP) committee. He is a Co-chair of special sessions, Co-organizer of the S&YP Forum, and Co-chair of 3M video sessions in IES conferences. He is an Associate Editor for IEEE TRANSACTIONS ON INDUSTRIAL ELECTRONICSand IEEE OPEN JOURNAL OF INDUSTRIAL ELECTRONICS SOCIETY.